

光学学报

反射式赝热光源散斑场的三维特性研究

卢立斌^{1,3}, 谈志杰^{1*}, 喻虹^{1,2}, 韩申生^{1,2}

¹中国科学院上海光学精密机械研究所量子光学重点实验室, 上海 201800;

²国科大杭州高等研究院, 浙江 杭州 310024;

³中国科学院大学, 北京 100049

摘要 傅里叶变换关联成像通常采用透射式赝热光源, 但透射产生散斑的纵向尺寸过大限制了成像纵向分辨率且透射式赝热光的光通量较低, 这对实现三维傅里叶变换关联成像造成了阻碍。为解决这一问题, 理论推导了反射式赝热光源散斑场的光强涨落关联函数, 给出了散射屏放置在不同空间位置和倾斜角度时的纵向散斑尺寸。同时, 进行了基于统计光学的数值模拟, 模拟结果与理论结果吻合。结果表明, 通过减小散射角和增大散射屏方位角等方法可以有效降低观察点处的纵向散斑尺寸, 从而提高纵向成像分辨率。

关键词 成像系统; 散斑场; 蕨热光; 粗糙表面; 关联成像

中图分类号 O434.19

文献标志码 A

DOI: 10.3788/AOS221780

1 引言

关联成像又被称为鬼成像(GI), 最初是在量子光学领域利用纠缠光子实现的一种非定域成像技术^[1]。2002年, Bennink等^[2]使用经典热光源也实现了GI, 随后经典热光源关联成像得到了理论证明和实验验证^[3-5], 并在许多领域中实现了应用^[6-9]。2004年, Cheng等^[5]将GI拓展到X光成像领域, 提出了X光傅里叶变换关联成像(XFGI)的理论构想, 并于2007年在可见光波段进行了原理验证^[10]。相比于传统的X光成像技术如X光吸收成像、相衬成像^[11]和相干衍射成像^[12]等, XFGI作为一种新的高分辨X光成像技术, 具备光源相干性要求较低、抗干扰性强^[13]和超越经典衍射极限分辨率^[14]等优点, 因其全新的物理机制、独特的成像特性, 在生物医学、材料科学等许多领域中有着广阔的应用前景, 近年来受到了越来越多的关注^[15-18]。2016年, Yu等^[19]首次完成了XFGI的实验演示, 为XFGI的实际应用奠定了基础。随后, Zhang等^[16]于2018年用台式X射线源实现了超低辐射关联成像, 表明其在弱光成像上的优势。同年, Kingston等^[20]利用计算断层扫描(CT)的方法在低剂量下实现了三维X光强度关联成像, 相比于传统X光三维成像, 该实验体现出X光三维成像能够最大化地利用光强信息来提高图像质量并降低样品的辐射剂量。2019年, Cheng^[21]在一级玻恩近似下将XFGI推广到三维, 并以Gauss-

Schell模型光束作为光源进行了数值模拟, 为三维XFGI提供了理论依据。

目前FGI实验主要利用的光源是透射式赝热光源^[22], 要想利用这种光源实现三维FGI仍然面临许多挑战。成像的纵向分辨率受限于散斑纵向尺寸^[23], 同时透射赝热光光通量较低^[19], 降低了成像的质量。近年来, 粗糙表面反射产生的散斑场受到了越来越多的关注^[24-26]。相比于透射式赝热光源, 反射的方式提供了更多可设计调整的自由度为降低散斑场纵向尺寸提供了可能。通过掠入射等方式也可以提高反射光光通量, 进而提高成像质量。

本文研究了反射式赝热光源产生散斑场的二阶统计性质, 理论推导了散射屏放置在不同空间位置和倾斜角时观察点纵向散斑尺寸的变化, 给出了降低反射式赝热光源纵向散斑尺寸的几种方法。同时, 通过基于统计光学的数值模拟方法进行了验证, 所得结果与理论结果吻合。通过改变散射屏的尺寸、空间位置和倾斜角度可以有效降低散斑场的纵向散斑尺寸, 进而提高成像的纵向分辨率。

2 理论模型和分析

反射式赝热光源示意图如图1(a)所示。均匀光束斜入射到粗糙散射屏上, 被反射后在空间中形成散斑场。图1(b)为对应图1(a)建立的坐标系统。为了方便, 仅讨论xz平面的散斑场特性, y方向分析同理。

收稿日期: 2022-09-30; 修回日期: 2022-11-03; 录用日期: 2022-11-25; 网络首发日期: 2023-01-04

基金项目: 国家重点研发计划(2017YFB0503303)、国家自然科学基金(11627811)

通信作者: *tanzj@siom.ac.cn

以空间中观察点 o_p 为坐标原点建立直角坐标系 o_p-xz ,并设散射屏的中心点 o_s 的坐标为 (x_s, z_s) ,法向 \mathbf{n} 与 x 方向倾角为 θ_s 。入射光束沿入射光方向矢量 i 方向照射在散射屏上形成散斑场,被照射的散射屏尺寸为 L ,入射光方向的改变会在一定程度上影响 L 。散射光沿

散射光方向矢量 e 传播到观察点 o_p 区域。待测样品放置在观察点 $o_p(0, 0)$ 位置,其横向和纵向位置分别为 x 方向和 z 方向,通过改变散射屏的位置和倾斜角度,待测样品位置处就可以获得不同的纵向散斑尺寸,从而改变成像的纵向分辨率。

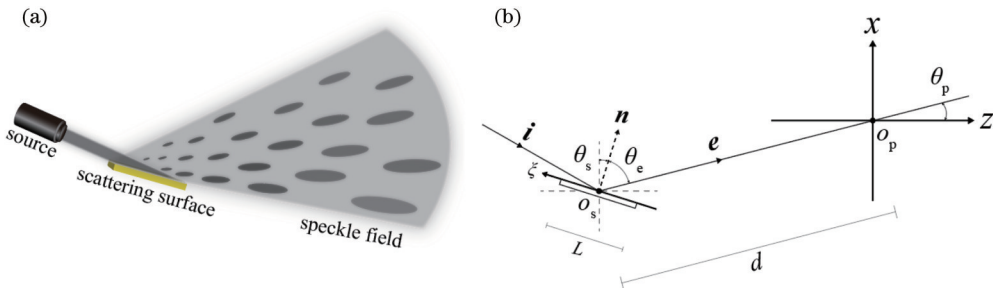


图1 反射式赝热光源。(a)示意图;(b)坐标系统

Fig. 1 Reflective pseudo-thermal light source. (a) Schematic diagram; (b) coordinate system

通常传播距离远大于散射屏的尺度,在该情况下观察点 o_p 临近区域的散斑场复振幅分布 U_p 可以由菲涅耳积分^[27-28]表示为

$$U_p(x, z) = \frac{1}{\sqrt{i\lambda(d + \Delta d)}} \int U_s(\xi) \exp\left[-\frac{ik}{2(d + \Delta d)} (\rho - \xi \cos \theta_e)^2\right] d\xi, \quad (1)$$

其中

$$\begin{cases} d = \sqrt{x_s^2 + z_s^2}, \\ \theta_p = \arctan \frac{x_s}{z_s} \\ \theta_e = \frac{\pi}{2} - \theta_s - \theta_p \\ \Delta d = (z + x \tan \theta_p) \cos \theta_p \\ \rho = (x - z \tan \theta_p) \cos \theta_p \end{cases}, \quad (2)$$

式中: ξ 为散射屏上的位置坐标; λ 为入射光波长; k 为入射光束波数; d 为散射屏中心到观察点的传播距离; θ_e 为散射屏相对于观察点的散射角,该值可以反映散射屏的倾斜角; θ_p 为散射屏方位角,即散射光方向矢量 e 和 z 方向的夹角,该值可以反映散射屏的空间位置。改变 θ_p 、 d 和 θ_e 可以改变散射屏的空间位置和倾斜角度。紧贴散射屏处的散射光复振幅分布 $U_s(\xi)$ ^[29]可以近似表示为

$$U_s(\xi) = U_i(\xi) \exp[k(-i \cdot n + e \cdot n) h(\xi)], \quad (3)$$

式中: $U_i(\xi)$ 为入射到散射屏上的复振幅分布; $h(\xi)$ 为散射屏的表面高度分布。

观察点 $o_p(0, 0)$ 与其临近点 (x, z) 的光强涨落关联函数 $\Delta G^{(2)}(x, z)$ ^[23]的定义为

$$\Delta G^{(2)}(x, z) = \langle \Delta I(0, 0) \Delta I(x, z) \rangle = \langle I(0, 0) I(x, z) \rangle - \langle I(0, 0) \rangle \langle I(x, z) \rangle, \quad (4)$$

式中: $I(x, z)$ 为坐标 (x, z) 处的光场强度; $\Delta I(x, z) = I(x, z) - \langle I(x, z) \rangle$ 为 (x, z) 处的光场强度与平均光场强度的差值; $\langle \cdot \rangle$ 为系综平均运算。假设散射屏表面高度服从高斯随机分布,且认为散射屏发出的散射光的光强分布是均匀的,则紧贴散射屏处的散射光复振幅分布 $U_s(\xi)$ ^[30-31]满足

$$\langle U_s(\xi_1) U_s^*(\xi_2) \rangle = \bar{I} \delta(\xi_1 - \xi_2), \quad (5)$$

式中: \bar{I} 为紧贴散射屏处的散射光平均光强; $U_s^*(\xi_2)$ 为 $U_s(\xi)$ 的复共轭; $\delta(\xi_1 - \xi_2)$ 为狄拉克函数。根据以上假设和高斯矩定理,在观察区域的散斑场^[30]满足

$$\langle I(0, 0) I(x, z) \rangle = \langle I(0, 0) \rangle \langle I(x, z) \rangle + \left| \langle U_p(0, 0) U_p^*(x, z) \rangle \right|^2. \quad (6)$$

将式(1)、式(5)和式(6)代入式(4)中有

$$\Delta G^{(2)}(x, z) = \left| \langle U_p(0, 0) U_p^*(x, z) \rangle \right|^2 = \frac{\bar{I}^2}{\lambda^2 d (d + \Delta d)} \left| \int \exp\left[\frac{ik}{2(d + \Delta d)} (\xi \cos \theta_e - \rho)^2 - \frac{ik}{2d} (\xi \cos \theta_e)^2 \right] d\xi \right|^2, \quad (7)$$

当 $d \gg \Delta d$ 时,对式(7)可以进行近似处理^[28]得到

$$\Delta G^{(2)}(x, z) \propto \left| \int \exp \left[-\frac{ik\Delta d}{2d^2} (\xi \cos \theta_e)^2 - \left(1 - \frac{\Delta d}{d} \right) \frac{ik\rho}{d} \xi \cos \theta_e \right] d\xi \right|^2. \quad (8)$$

散斑场的散斑尺寸 l 的本质为散斑场在空间中相干区域的大小,可以定义为归一化光强涨落关联函数 $\Delta g^{(2)}(x, z)$ 的半峰全宽^[23]。因此,通过计算式(8)关于坐标空间的归一化半峰全宽,便可求得方位角为 θ_p 、传播距离为 d 且散射角为 θ_e 的散射屏产生的散斑场在观察点 o_p 处的散斑尺寸。然而,一般情况下式(8)不存在解析解,为了分析如何降低观察点 o_p 处沿纵向方向即 z 方向的散斑尺寸 l_z ,下面给出了两种特殊情况下观察点处纵向散斑尺寸的近似值。

首先,考虑散射屏相对于观察点的散射方向沿观察点纵向方向时的情况,即 $\theta_p = 0^\circ, x = 0$ 的情况,此时 $\rho = 0$,进而式(8)可以化简为

$$\Delta G^{(2)}(x=0, z) \propto \left| \int \exp \left[-\frac{ikz}{2d^2} (\xi \cos \theta_e)^2 \right] d\xi \right|^2, \quad (9)$$

对应的归一化光强涨落关联函数最终可以表示为

$$\Delta g^{(2)}(x=0, z) = \left| \sqrt{\frac{2\pi}{Az}} \left[C\left(\sqrt{\frac{Az}{2\pi}}\right) + iS\left(\sqrt{\frac{Az}{2\pi}}\right) \right] \right|^2, \quad (10)$$

式中: $A = \pi L^2 / (\lambda d^2)$; $C(z)$ 和 $S(z)$ 分别为菲涅耳余弦和正弦积分。散射屏散射方向沿纵向方向时产生的散斑场的纵向散斑尺寸即为式(10)的半峰全宽,可近似为

$$l_z \approx 6.98\lambda \left(\frac{d}{L \cos \theta_e} \right)^2. \quad (11)$$

由式(11)对比Goodman^[29]在散射屏与观察面平行的情况下给出的深度方向上的散斑尺寸理论可以看到,散射屏在不同散射方向的散斑尺寸等效于在该方向上投影出的散射屏所产生的散斑尺寸。因此,当散射屏方位角为 $\theta_p = 0^\circ$ 且传播距离 d 固定时,减小散射角 θ_e 便可以减小观察点处的纵向散斑尺寸。

然后,考察散射屏相对于观察点的散射方向偏离观察点纵向一定角度的情况。满足条件

$$\frac{\pi L^2 \Delta d}{d^2} \ll \lambda, \quad (12)$$

式(8)可以化简为

$$\Delta G^{(2)}(x, z) \propto \left| \int \exp \left[-\frac{ik\rho}{d} \xi \cos \theta_e \right] d\xi \right|^2, \quad (13)$$

则对应的归一化光强涨落关联函数可以表示为

$$\Delta g^{(2)}(x, z) = \text{sinc}^2 \left(\frac{L\rho \cos \theta_e}{\lambda d} \right), \quad (14)$$

该函数在 $x=0$ 时关于 z 的半峰全宽即散斑场在观察点 o_p 处的纵向散斑尺寸可以近似为

$$l_z \approx 0.885\lambda \frac{d}{L \sin \theta_p \cos \theta_e}. \quad (15)$$

由式(11)和式(15)可得,对于一个确定的观察点,反射式赝热光系统对其的纵向散斑尺寸与入射光波长、散射屏尺寸、散射屏放置的空间位置和倾斜角度有关。因此,在不更换成像系统器件的情况下,可以通过4种方法来减小赝热光源在观察点处纵向方向的散斑尺寸,从而提高观察点区域成像的纵向分辨能力,即增大散射屏尺度 L 、增大散射屏方位角 θ_p 、缩短传播距离 d 和减小散射角 θ_e 。

3 数值仿真与讨论

为进一步探究散射屏在不同空间位置和倾斜角度时纵向散斑尺寸的变化,利用计算机对粗糙散射屏产生的散斑场进行了数值仿真模拟,并对其二阶统计性质进行了分析。仿真中取散射屏粗糙度为 $20\mu\text{m}$,随着该尺寸的减小,散斑场的范围将增大^[32]。根据式(3),紧贴散射屏处的散射光相位分布满足 $0\sim 2\pi$ 范围内的均匀分布^[33]。因此,可以通过计算机生成相位均匀分布的散射光复振幅分布,再根据菲涅耳积分衍射理论计算出传播到观察点邻近区域散斑场的光场强度分布。重复上述过程得到多幅散斑场的光强分布以实现多次采样,并根据式(4)求得系综平均下观察点与其临近区域的归一化光强涨落关联函数,其在纵向和横向方向的半峰全宽分别为纵向和横向的散斑尺寸。

数值仿真中取入射光波波长为 $\lambda = 670\text{ nm}$,散射屏的尺寸为 $L = 25.4\text{ mm}$,采样点数 N 为2048。首先,考虑传播距离为 $d = 300\text{ mm}$,散射屏方位角为 $\theta_p = 0^\circ$,即散射屏中心点 o_s 在 z 轴上的情况,当散射屏倾角为 $\theta_s = 50^\circ$ 时,散射角为 $\theta_e = 40^\circ$,计算得到观察点临近区域不同传播距离 d 下散斑场光强分布,如图2(a)所示。通过多次生成散斑场实现多次采样,以计算观察点与其临近区域的归一化光强涨落关联函数 $\Delta g^{(2)}$ 。1500次采样后得到的观察点纵向和横向的 $\Delta g^{(2)}$ 的变化分别如图2(b)和图2(c)所示。为了验证理论的正确性,将上述物理参数代入式(8)中计算得到观察点与临近区域的归一化光强涨落关联函数分布,并将其与1500次采样后系综平均数值模拟结果进行比较,如图3所示。图3展示了 $\Delta g^{(2)}(x, z)$ 的强度变化理论结果,用黑色虚线标出了 $\Delta g^{(2)}$ 分别为0.7、0.5和0.3时的等高线,并用“+”、“×”和“.”标出了 $\Delta g^{(2)}$ 对应数值仿真结果的空间位置。可以看到,理论结果和数值仿真结果基本一致,但由于数值仿真结果为有限次采样,故与理论结果存在细微差异。从图3可以看到,当散射屏方位角为 $\theta_p = 0^\circ$ 时,观察点处沿纵向方向的

$\Delta g^{(2)}$ 的半峰全宽为 1.102 mm 远大于其他方向, 即散射屏产生的散斑沿散射方向的长度最长, 越偏离散射

方向散斑尺寸越小。因此, 增大散射屏方位角可以减小纵向散斑尺寸。

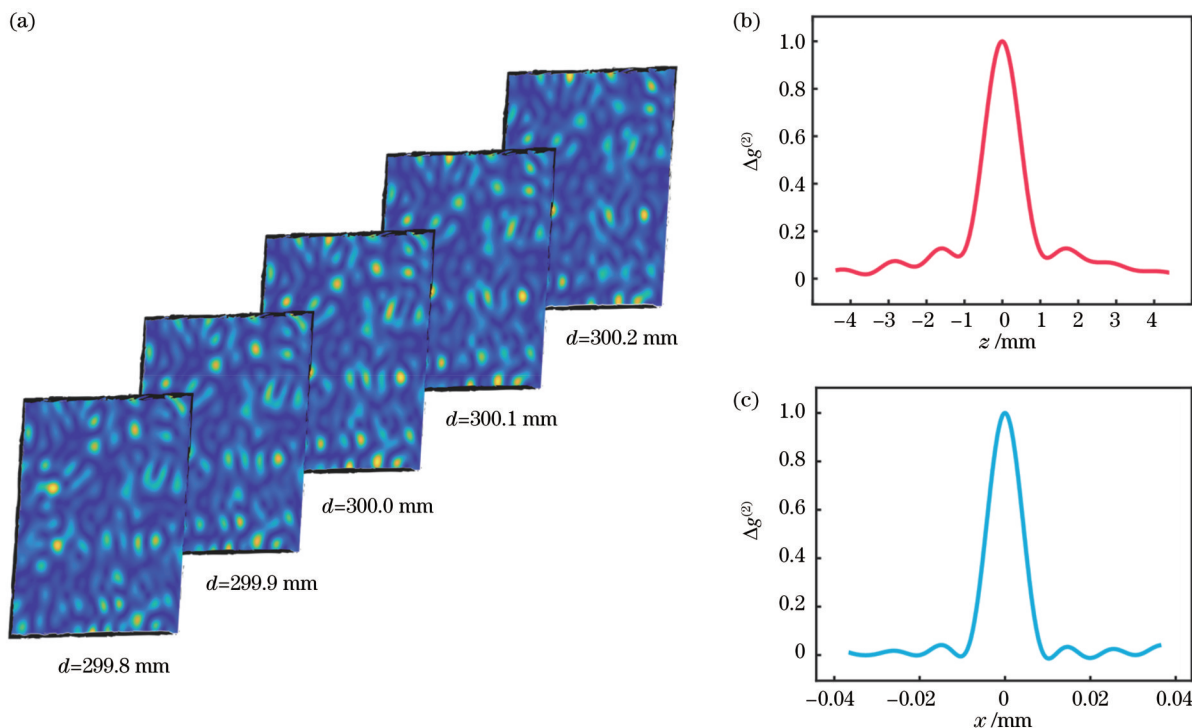


图 2 散斑场数值仿真结果。(a)光强分布;(b)纵向二阶关联函数;(c)横向二阶关联函数

Fig. 2 Numerical simulation results of speckle field. (a) Intensity distribution; (b) longitudinal second-order correlation function; (c) transverse second-order correlation function

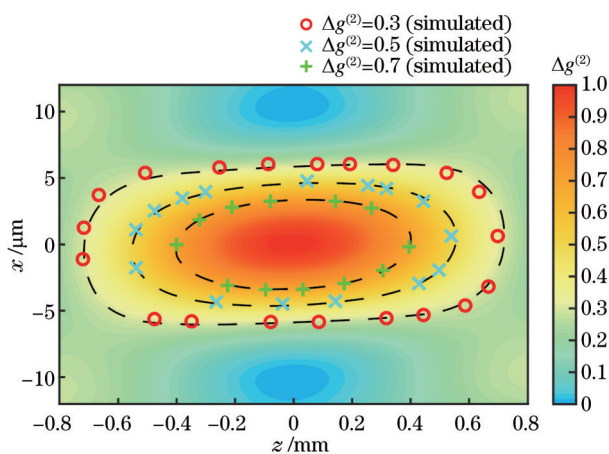


图3 归一化光强涨落关联函数的理论结果和数值仿真结果对比

Fig. 3 Comparison of theoretical and numerical simulation results of normalized intensity fluctuation correlation function

图 4 进一步说明了影响散斑场在观察点处纵向散斑尺寸各项因素的作用。图 4(a)为不同散射屏尺寸 L 下传播距离 d 和纵向散斑尺寸 l_z 的关系。保持散射屏方位角 $\theta_p = 0^\circ$ 和散射角 $\theta_e = 40^\circ$ 不变, 可以看到: 当 $L = 101.6 \text{ mm}$ 、 $d = 600 \text{ mm}$ 时, $l_z \approx 27.19 \text{ mm}$; 当 $L = 25.4 \text{ mm}$ 、 $d = 600 \text{ mm}$ 时, $l_z \approx 4.436 \text{ mm}$; 当 $L = 101.6 \text{ mm}$ 、 $d = 200 \text{ mm}$ 时, $l_z \approx 0.02679 \text{ mm}$ 。因此,

纵向散斑尺寸随着传播距离的减小和散射屏尺寸的增大而不断减小。图 4(b)为不同散射角 θ_e 下散射屏方位角 θ_p 与纵向散斑尺寸 l_z 的关系。保持 $L = 25.4 \text{ mm}$ 和 $d = 300 \text{ mm}$ 不变, 可以看到: 当 $\theta_p = 5^\circ$ 、 $\theta_e = 50^\circ$ 时, $l_z \approx 126.0 \mu\text{m}$; 当 $\theta_p = 5^\circ$ 、 $\theta_e = 20^\circ$ 时, $l_z \approx 85.84 \mu\text{m}$; 当 $\theta_p = 15^\circ$ 、 $\theta_e = 50^\circ$ 时, $l_z \approx 42.23 \mu\text{m}$ 。因此, 纵向散斑尺寸随着散射屏倾斜角的减小和散射屏方位角的增大而不断减小, 与理论分析的结果一致。值得注意的是, 由于散斑在散射方向的尺寸远大于其他方向, 故纵向散斑尺寸随散射屏方位角在 0° 附近的变化率很大, 而在散射屏方位角较大时的变化率较小。

对于 X 光波段, 采用掠入射的方式入射到散射屏上, 能够提高散射光光通量^[34-35]。当入射光波波长为 0.1 nm 时, 对硅散射屏的全反射临界角(入射光线与散射屏平面的夹角)约为 0.14° ^[36]。在这种情况下照射在硅散射屏上的入射角和反射角趋近于 90° ^[37], 故主要通过调整散射屏大小和散射屏方位角来减小观察点处的纵向散斑尺寸。取入射光波波长为 0.1 nm、入射光束宽度为 $50 \mu\text{m}$ 、入射角为 89.86° 、散射角为 89.86° 和传播距离为 20 mm, 不同散射屏尺寸 L 和不同散射屏方位角 θ_p 与纵向散斑尺寸 l_z 的理论关系曲线如图 5 所示。当 $L = 20 \text{ mm}$ 、 $\theta_p = 20^\circ$ 时, 理论结果仍成立: 观察点处的纵向散斑尺寸可以达到 100 nm 以下(约为

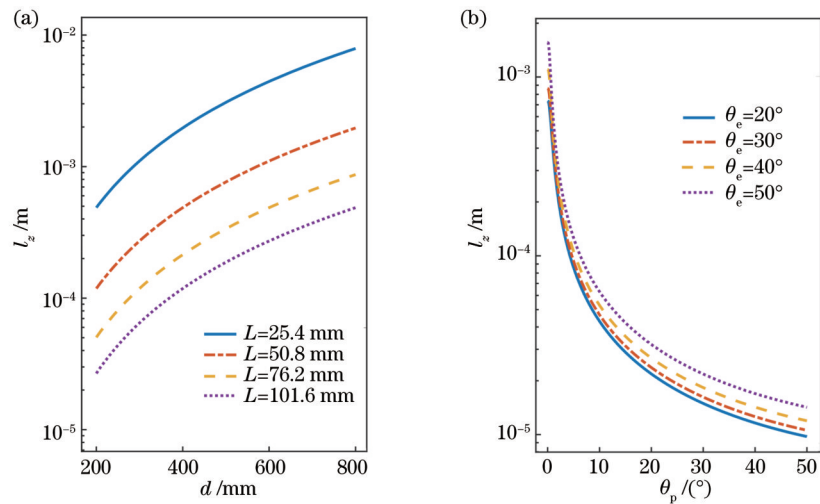


图4 纵向散斑尺寸 l_z 的理论结果。(a)不同 L 下 d 和 l_z 的关系;(b)不同 θ_e 下 θ_p 和 l_z 的关系

Fig. 4 Theoretical results of longitudinal speckle size l_z . (a) Relationship between d and l_z under different L ; (b) relationship between θ_p and l_z under different θ_e .

79.31 nm);观察点处的横向散斑尺寸(沿 x 方向的散斑尺寸)约为28.94 nm。

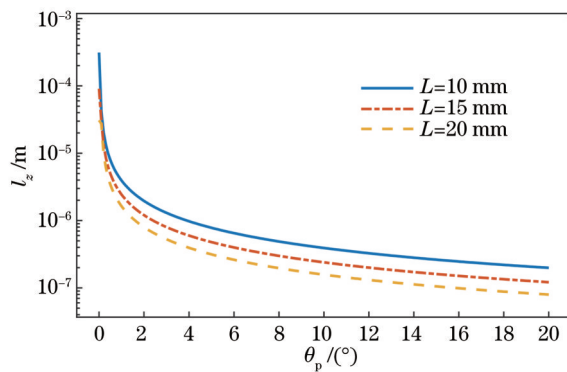


图5 X光波段中不同 L 下 θ_p 与 l_z 的关系

Fig. 5 Relationship between θ_p and l_z under different L in X-ray band

4 结 论

研究了反射式赝热光源产生散斑场的二阶统计性质,从理论上推导了粗糙散射屏产生散斑场在观察点与其相邻区域的光强涨落关联函数表达式。给出了散射屏散射方向沿观察点纵向和偏离纵向一定角度时观察点处纵向散斑尺寸的近似值,并进行了基于统计光学的数值模拟仿真,仿真与理论结果基本一致。散射屏尺寸、空间位置和倾斜状态会影响观察点的散斑尺寸。入射光波波长越短,传播距离越近,则散斑尺寸越小。增大散射屏尺寸和减小散射角可以增大散射方向的投影散射屏大小,从而减小散斑尺寸。此外,由于沿散射方向的散斑尺寸远大于其他方向,因此纵向散斑尺寸随散射屏方位角的增大而减小,且在低角度时纵向散斑尺寸的变化率很大。最后,给出了X光波段反射式赝热光源不同参数情况对应的纵向散斑尺寸,通

过合理设计散射屏的空间位置和倾斜角度可以有效降低观察点处的纵向散斑尺寸达到100 nm以下,从而提高纵向的成像分辨率,这对三维XFGI的发展具有重要意义。

参 考 文 献

- [1] Pittman T B, Shih Y H, Strekalov D V, et al. Optical imaging by means of two-photon quantum entanglement[J]. Physical Review A, 1995, 52(5): R3429-R3432.
- [2] Bennink R S, Bentley S J, Boyd R W. Two-Photon coincidence imaging with a classical source[J]. Physical Review Letters, 2002, 89(11): 113601.
- [3] Cai Y J, Zhu S Y. Ghost interference with partially coherent radiation[J]. Optics Letters, 2004, 29(23): 2716-2718.
- [4] Gatti A, Brambilla E, Bache M, et al. Ghost imaging with thermal light: comparing entanglement and classical correlation [J]. Physical Review Letters, 2004, 93(9): 093602.
- [5] Cheng J, Han S S. Incoherent coincidence imaging and its applicability in X-ray diffraction[J]. Physical Review Letters, 2004, 92(9): 093903.
- [6] Zhang M H, Wei Q, Shen X, et al. Sub-wavelength Fourier-transform imaging of a pure-phase object with thermal light[J]. Physics Letters A, 2007, 366(6): 569-574.
- [7] Cheng J, Lin J. Unified theory of thermal ghost imaging and ghost diffraction through turbulent atmosphere[J]. Physical Review A, 2013, 87(4): 043810.
- [8] Xu Y K, Liu W T, Zhang E F, et al. Is ghost imaging intrinsically more powerful against scattering? [J]. Optics Express, 2015, 23(26): 32993-33000.
- [9] 谈志杰, 尹少齐, 喻虹, 等. 基于空间调制的星体观测张角强度关联干涉测量[J]. 光学学报, 2022, 42(7): 0712005.
- Tan Z J, Yin S Q, Yu H, et al. Intensity correlation interferometry for astral observation angle based on spatial modulation[J]. Acta Optica Sinica, 2022, 42(7): 0712005.
- [10] Zhang M H, Wei Q, Shen X, et al. Lensless Fourier-transform ghost imaging with classical incoherent light[J]. Physical Review A, 2007, 75(2): 021803.
- [11] Davis T J, Gao D, Gureyev T E, et al. Phase-contrast imaging of weakly absorbing materials using hard X-rays[J]. Nature, 1995, 373(6515): 595-598.
- [12] Fan J D, Sun Z B, Zhang J, et al. Quantitative imaging of single

- unstained magnetotactic bacteria by coherent X-ray diffraction microscopy[J]. Analytical Chemistry, 2015, 87(12): 5849-5853.
- [13] Lane T J, Ratner D. What are the advantages of ghost imaging? Multiplexing for X-ray and electron imaging[J]. Optics Express, 2020, 28(5): 5898-5918.
- [14] Xiong J, Cao D Z, Huang F, et al. Experimental observation of classical subwavelength interference with a pseudo-thermal light source[J]. Physical Review Letters, 2005, 94(17): 173601.
- [15] Pelliccia D, Rack A, Scheel M, et al. Experimental X-ray ghost imaging[J]. Physical Review Letters, 2016, 117(11): 113902.
- [16] Zhang A X, He Y H, Wu L A, et al. Tabletop X-ray ghost imaging with ultra-low radiation[J]. Optica, 2018, 5(4): 374-377.
- [17] Kingston A M, Myers G R, Pelliccia D, et al. X-ray ghost-tomography: artefacts, dose distribution, and mask considerations[J]. IEEE Transactions on Computational Imaging, 2019, 5(1): 136-149.
- [18] 谈志杰, 李晴宇, 喻虹, 等. X射线及粒子关联成像技术研究进展[J]. 激光与光电子学进展, 2021, 58(10): 1011008.
Tan Z J, Li Q Y, Yu H, et al. Progress on ghost imaging with X-ray and particles[J]. Laser & Optoelectronics Progress, 2021, 58(10): 1011008.
- [19] Yu H, Lu R H, Han S S, et al. Fourier-transform ghost imaging with hard X rays[J]. Physical Review Letters, 2016, 117(11): 113901.
- [20] Kingston A M, Pelliccia D, Rack A, et al. Ghost tomography [J]. Optica, 2018, 5(12): 1516-1520.
- [21] Cheng J. Weak ghost scattering with stochastic electromagnetic beams[J]. OSA Continuum, 2019, 2(2): 268-278.
- [22] 陈倩, 喻虹, 谈志杰, 等. X光超瑞利散斑场傅里叶变换关联成像模拟研究[J]. 光学学报, 2021, 41(19): 1934001.
Chen Q, Yu H, Tan Z J, et al. Simulation research on X-ray Fourier-transform ghost imaging using super-Rayleigh speckle field[J]. Acta Optica Sinica, 2021, 41(19): 1934001.
- [23] Liu H L, Han S S. Spatial longitudinal coherence length of a thermal source and its influence on lensless ghost imaging[J]. Optics Letters, 2008, 33(8): 824-826.
- [24] Zhang G, Wu Z S. Bi-frequency correlation properties of the scattered intensity from dielectric rough surfaces[J]. Optics Express, 2012, 20(14): 14833-14847.
- [25] Wang Z, Sanders S T. Toward single-ended absorption spectroscopy probes based on backscattering from rough surfaces: H_2O vapor measurements near 1350 nm[J]. Applied Physics B, 2015, 121(2): 187-192.
- [26] Divitt S, Watnik A T. Spatial-spectral correlations of broadband speckle in around-the-corner imaging conditions[J]. Optics Express, 2022, 30(5): 7169-7186.
- [27] Wang C F, Zhang D W, Bai Y F, et al. Ghost imaging for a reflected object with a rough surface[J]. Physical Review A, 2010, 82(6): 063814.
- [28] Nan S Q, Bai Y F, Shi X H, et al. Experimental investigation of ghost imaging of reflective objects with different surface roughness[J]. Photonics Research, 2017, 5(4): 372-376.
- [29] Goodman J W. Speckle phenomena in optics: theory and applications[M]. Englewood: Roberts & Co., 2007.
- [30] Zhang G, Wu Z S, Li Y H. Speckle size of light scattered from 3D rough objects[J]. Optics Express, 2012, 20(4): 4726-4737.
- [31] Li Q B, Chiang F P. Three-dimensional dimension of laser speckle[J]. Applied Optics, 1992, 31(29): 6287-6291.
- [32] 郁魏柯, 杜小平, 王阳, 等. 微粗糙表面参数对激光散斑场的影响规律分析[J]. 光学学报, 2021, 41(11): 1103001.
Gao W K, Du X P, Wang Y, et al. Analysis of influences of micro-rough surface parameters on laser speckle field[J]. Acta Optica Sinica, 2021, 41(11): 1103001.
- [33] Leushacke L, Kirchner M. Three-dimensional correlation coefficient of speckle intensity for rectangular and circular apertures[J]. Journal of the Optical Society of America A, 1990, 7(5): 827-832.
- [34] Yu H, Lu R, Tan Z, et al. Recent progress in X-ray Fourier-transform ghost imaging[J]. Nuclear Instruments and Methods in Physics Research Section A: Accelerators, Spectrometers, Detectors and Associated Equipment, 2019, 928: 33-36.
- [35] Barton G. The quantum theory of light[J]. Physics Bulletin, 1974, 25(3): 103-104.
- [36] McMorrow D, Als-Nielsen J. Elements of modern X-ray physics [M]. 2nd ed. Hoboken: Wiley, 2011.
- [37] Hayashi K. Review of the applications of X-ray refraction and the X-ray waveguide phenomenon to estimation of film structures[J]. Journal of Physics: Condensed Matter, 2010, 22(47): 474006.

Three-Dimensional Characteristics of Speckle Field of Reflective Pseudothermal Light Sources

Lu Libin^{1,3}, Tan Zhijie^{1*}, Yu Hong^{1,2}, Han Shensheng^{1,2}

¹Key Laboratory of Quantum Optics, Shanghai Institute of Optics and Fine Mechanics, Chinese Academy of Sciences, Shanghai 201800, China;

²Hangzhou Institute for Advanced Study, University of Chinese Academy of Sciences, Hangzhou 310024, Zhejiang, China;

³University of Chinese Academy of Sciences, Beijing 100049, China

Abstract

Objective X-ray Fourier-transform ghost imaging (XFGI) is a new imaging technology that has emerged in recent years. Unlike traditional X-ray imaging, the resolution limit of this imaging method is theoretically limited only by the X-ray wavelength, which makes it possible to obtain higher spatial resolution than real-space imaging. Moreover, the phase information of the sample can also be obtained by this technique, which is of great significance for the imaging of weakly absorbing biological samples. However, the current FGI experiments mainly utilize transmissive pseudo-thermal light sources. The longitudinal size of the speckle generated by the transmissive source is too large, which limits the

longitudinal resolution of imaging. Meanwhile, the luminous flux of transmissive pseudo-thermal light is low, which makes it difficult to carry out three-dimensional FGI. In contrast, the reflection method can provide more room for design and adjustment, allowing the longitudinal size of the speckle to be reduced. Furthermore, grazing incidence can be used to increase the reflected light flux and hence improve imaging quality. Therefore, the three-dimensional characteristics of the speckle field of the reflective pseudo-thermal light source are studied in hope of guiding and improving the light source system of three-dimensional FGI and thereby enhancing the longitudinal imaging resolution.

Methods According to the Fresnel diffraction theory, the position of the pending sample is taken as the observation position, and the correlation function of the intensity fluctuation of the speckle field emitted by the scattering screen is derived. The speckle size is defined as the full width at half maximum of the speckle field. The longitudinal speckle size of speckle fields emitted by scattering screens at different spatial positions and inclination angles is discussed. Then, the numerical simulation based on statistical optics is carried out in the visible light region. Through the simulation, the light-field intensity distribution of the speckle field is obtained, and the normalized light intensity fluctuation correlation function between the observation position and its adjacent area under the ensemble average is calculated to verify the theoretical results. Moreover, various factors affecting the longitudinal speckle size at the observation position of the speckle field are analyzed, such as the size of the scattering screen, propagation distance, scattering angle, and azimuth angle. Finally, for high-resolution three-dimensional XFGI, the longitudinal speckle size of the grazing-incidence silicon scattering screen reflective pseudo-thermal light source is also considered.

Results and Discussions From the point of view of statistical optics, the longitudinal speckle size of speckle fields emitted by scattering screens at different spatial positions and inclination angles is given, which is consistent with the numerical simulation results under the ensemble average (Fig. 3). In the visible light region, the influence of various factors on the longitudinal speckle size at the observation position is discussed and numerically simulated (Fig. 4). The longitudinal speckle size can be effectively reduced by the following four strategies, i. e., increasing the size of the scattering screen, increasing the azimuth angle of the scattering screen, shortening the propagation distance, and reducing the scattering angle. In the end, the longitudinal speckle size at the observation position is decreased to less than 100 nm under the rational design of the spatial position and inclination angles of the silicon scattering screen in the X-ray region. When the wavelength of the incident light wave is 0.1 nm, the size of the silicon scattering screen is 20 mm, the incident angle and the scattering angle are both 89.86°, the azimuth angle of the scattering screen is 20°, and the propagation distance is 20 mm, the longitudinal speckle size at the observation position can reach 79.31 nm, and the lateral speckle size can reach 28.94 nm (Fig. 5).

Conclusions In this paper, the second-order statistical characteristics of the speckle field generated by the reflective pseudo-thermal light source are studied, and the intensity fluctuation correlation function of the speckle field of the reflective pseudo-thermal light source is theoretically derived. In addition, the longitudinal speckle size of the scattering screen placed at different spatial positions and inclination angles is given. The numerical simulation results based on the statistical optics are consistent with the theoretical results. The results show that the size, spatial position, and tilt state of the scattering screen will affect the speckle size at the observation position. The size of the speckle decreases with both the incident light wave's wavelength and the propagation distance. The size of the projection scattering screen in the scattering direction can be increased, which will reduce the size of speckles under a larger scattering screen and a smaller scattering angle. Moreover, the longitudinal speckle size decreases with the increasing azimuth of the scattering screen and changes abruptly at small angles since the speckle size along the scattering path is significantly bigger than that in other directions. Finally, the longitudinal speckle size of the reflective pseudo-thermal light source under different parameters is given in the X-ray region. The longitudinal speckle size at the observation position can be effectively reduced to less than 100 nm under the rational design of the spatial position and inclination angle of the scattering screen. In this way, the longitudinal resolution of imaging can be improved, which is of great significance for the development of three-dimensional FGI.

Key words imaging systems; speckle field; pseudo-thermal light; rough surface; ghost imaging